

# Control over Light Emission in Low-Refractive-Index Artificial Materials Inspired by Reciprocal Design

Lukas Maiwald, Timo Sommer, Mikhail S. Sidorenko, Ruslan R. Yafyasov, Meraj E. Mustafa, Marvin Schulz, Mikhail V. Rybin, Manfred Eich, and Alexander Yu. Petrov\*

Reciprocal space engineering allows tailoring the scattering response of media with a low refractive-index contrast. Here it is shown that a quasiperiodic leveled-wave structure with well-defined reciprocal space and random real space distribution can be engineered to open a complete photonic bandgap (CPBG) for any refractive-index contrast. For these structures, an analytical estimation is derived, which predicts that there is an optimal number of Bragg peaks for any refractive-index contrast. A finite 2D or 3D CPBG is expected at this optimal number even for an arbitrarily small refractive-index contrast. Results of numerical simulations of dipole emission in 2D and 3D structures support the estimations. In 3D simulations, an emission suppression of almost 10 dB is demonstrated with a refractive index down to 1.38. The 3D structures are realized by additive manufacturing on millimeter scale for a material with a refractive index of  $n \approx 1.59$ . Measurements confirm a strong suppression of microwave transmission in the expected frequency range.

## 1. Introduction

The design of novel materials with unprecedented properties is a great challenge of modern science. Two types of rationally designed structured media for governing electromagnetic waves were established in recent decades: periodic media, referred to as photonic crystals (PhC),<sup>[1–4]</sup> and metamaterials, which are optical materials composed of photonic meta-atoms smaller than the optical wavelength.<sup>[5,6]</sup> Established design rules exist for these materials, but the periodicity of PhC and the strict size limitations of metamaterials limit the design space. Inverse design methods using numerical optimization,<sup>[7–10]</sup> including artificial intelligence,<sup>[11]</sup> are another possibility. These methods result in complicated distributions of

material that support the desired functionality, but they come at the cost of physical tangibility, making it very hard for humans to judge their efficiency. Disordered structures<sup>[12,13]</sup> bear a much higher complexity than PhCs and metamaterials, but reciprocal space engineering might give a hint about how to utilize this complexity in a rational way. In a similar way, holography techniques make it possible to fabricate seemingly chaotic structures that modify a traversing wave front for a given image to appear. Due to the advances of 3D nanomanufacturing, many photonic structures utilizing tailored disorder have been demonstrated: hyperuniform structures,<sup>[14]</sup> photonic glasses,<sup>[15]</sup> quasicrystals,<sup>[16]</sup> Moiré lattices,<sup>[17]</sup> and Fourier surfaces.<sup>[18]</sup>

Incommensurate, quasiperiodic structures represent a special class of disordered systems where a high degree of order is present in reciprocal space. Recently, novel physical phenomena were discovered in Moiré lattices;<sup>[17]</sup> systems composed of a pair of similar lattices with different orientation. In particular, a transition between localization and delocalization was reported for photonic Moiré lattices. A pair of graphene flakes with arbitrary orientation effectively form similar systems for electrons.<sup>[19,20]</sup> However, the design space for atomic lattices is very limited in contrast to their photonic counterparts. In 2D, an overlap of multiple optical gratings forming incommensurate patterns was recently demonstrated for holographic projection.<sup>[18]</sup> One might design a structure by merging an arbitrary number of lattices even in full 3D space opening up with promising opportunities for novel photonic materials. A particularly challenging task is to obtain a complete photonic bandgap (CPBG). For a bandgap

L. Maiwald, M. E. Mustafa, M. Schulz, M. Eich, A. Yu. Petrov  
Institute of Optical and Electronic Materials  
Hamburg University of Technology  
21073 Hamburg, Germany  
E-mail: a.petrov@tuhh.de


T. Sommer  
Department of Physics  
Technical University Munich  
85748 Garching, Germany

T. Sommer  
Munich Center for Quantum Science and Technology (MCQST)  
80799 Munich, Germany

M. S. Sidorenko, R. R. Yafyasov, M. V. Rybin, A. Yu. Petrov  
Department of Physics and Engineering  
ITMO University  
Saint Petersburg 199034, Russia

M. V. Rybin  
Ioffe Institute  
Saint Petersburg 194021, Russia

M. Eich, A. Yu. Petrov  
Institute of Materials Research  
Helmholtz-Zentrum Hereon  
21502 Geesthacht, Germany

 The ORCID identification number(s) for the author(s) of this article can be found under <https://doi.org/10.1002/adom.202100785>.

© 2021 The Authors. Advanced Optical Materials published by Wiley-VCH GmbH. This is an open access article under the terms of the Creative Commons Attribution-NonCommercial License, which permits use, distribution and reproduction in any medium, provided the original work is properly cited and is not used for commercial purposes.

DOI: 10.1002/adom.202100785

to be complete, the individual direction-specific gaps related to the reciprocal vectors need to overlap over the full solid angle. This requires the interplay of two conditions: first, the Brillouin zone of the structures should be as close as possible to a circle in 2D and a spherical shell in 3D, so the individual gaps open for similar frequencies and cover all angles.<sup>[21–23]</sup> Second, a high-refractive-index (RI) contrast leads to wider individual gaps and can, therefore, compensate for residual deviations from the ideal circle or spherical shell shape. In this publication, we define the RI contrast as the ratio of the refractive indices of two constituent media,  $n_1/n_2$ , where  $n_1$  is larger than  $n_2$ , so that the minimal contrast is 1. To increase the range of available materials for PBG applications, there have been considerable efforts to minimize the required RI contrast employing periodic<sup>[4,22–26]</sup> and aperiodic<sup>[21,27–35]</sup> structures. As aperiodic structures are not limited by the crystallographic theorem and thus are allowed for a more flexible positioning of Bragg peaks and smoother effective Brillouin zones, they are generally considered superior for low-contrast CPBGs.

Here we report on artificial low-refractive-index media with a complete photonic bandgap. The medium is engineered in reciprocal space by merging a large number of lattices with proper spatial orientation into a single quasiperiodic structure. Tens of lattices form a nearly homogeneous distribution of the maxima in reciprocal space allowing a remarkable reduction of the RI contrast required for a CPBG. In real space, the leveled-wave approach is used to obtain structures made of a single material. The approach is somewhat similar to the holographic dual-beam exposure technique<sup>[33–37]</sup> but with random phase shifts between the individual lattices in our case.<sup>[38,39]</sup> This randomization leads to isotropic structures and allows us to draw important conclusions about the connection between the total RI contrast and the directional bandgaps. Based on that, we present a mathematical first-order approximation that yields two important results: there is a finite optimal number of gratings for any finite available RI contrast, and a CPBG can be obtained for any, even arbitrarily small, RI contrast. The predictions of the model are confirmed by numerical simulations in 2D. The same design rule proves successful in 3D where an unprecedented emission suppression of  $-10$  dB is shown with an RI contrast of  $n_1/n_2 = 1.38$ . A strong suppression of light transport is also confirmed in microwave transmission measurements conducted on a 3D-printed structure with an RI contrast of  $n_1/n_2 = 1.59$ .

## 2. Quasiperiodic Model Structure

The structures are generated by a superposition of sinusoidal 1D gratings, which have their normal directions homogeneously distributed over the whole angular range. For the 2D case, this can easily be realized by a uniform distribution over the azimuthal angle. 3D structures need a more complex distribution of gratings, which is described later. The superposition is mathematically described by a gradual function

$$\Delta n_g(\mathbf{r}) = \sum_{i=1}^N \Delta n_i \cos(\mathbf{b}_i \cdot \mathbf{r} + \phi_i) \quad (1)$$

where  $N$  is the total number of gratings,  $\Delta n_i$  is the amplitude of the RI modulation of a single grating,  $\mathbf{b}_i$  are the wave vectors

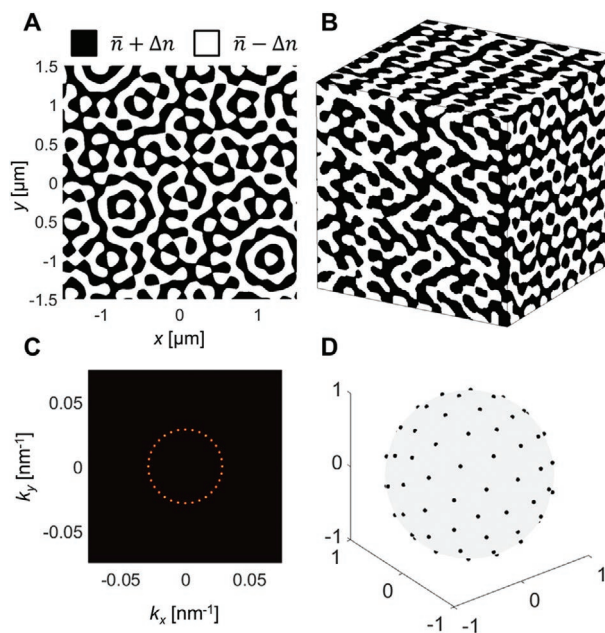


**Figure 1.** Quasiperiodic structures in real as well as reciprocal space. A,B) Examples of the investigated structures in 2D and 3D, respectively. The side lengths in both cases are  $\approx 13$  lattice constants  $a$ . The 2D image was generated based on an overlap of 16 gratings; the 3D image is based on 46 gratings. C) Squared Fourier transform of a circular excerpt of a 2D structure. D) Schematic representation of the Bragg peaks used for the 3D structure.

defining the grating periods and directions, and  $\phi_i$  are the corresponding phases. Since the Fourier transform is a linear operation, a summation of 1D gratings corresponds to a summation of the Fourier transforms of each grating. In this case, the cosine functions correspond to two Dirac delta functions, Bragg peaks, at  $\pm \mathbf{b}_i$  in reciprocal space. The same period  $a$ , and thus, lattice vector length  $b = |\mathbf{b}_i| = 2\pi/a$  and amplitude  $\Delta n_i$  is used for each grating. The phases  $\phi_i$  are chosen randomly. In this case, for a large number of gratings, the local RI perturbation has a Gaussian distribution with standard deviation  $\sigma_g = \Delta n_i(N/2)^{1/2}$  (see Section S1 in the Supporting Information).

To obtain a binary structure that can be represented by two materials, the sum in Equation (1) is then binarized by a sign function<sup>[34–38]</sup>

$$n_b(\mathbf{r}) = \bar{n} + \Delta n \cdot \text{sgn}(\Delta n_g(\mathbf{r})) \quad (2)$$

where  $\bar{n}$  is the mean refractive index,  $\Delta n$  is the amplitude of the refractive-index perturbation from the average value  $\bar{n}$ , thus  $n_1 = \bar{n} + \Delta n$  and  $n_2 = \bar{n} - \Delta n$ . We choose the perturbation strength to be equal to the standard deviation of the graded structure,  $\Delta n = \sigma_g$ . Two examples of the structures in 2D and 3D are presented in **Figure 1**. In contrast to previous works,<sup>[34–37]</sup> random phases  $\phi_i$  allow us to analytically evaluate the strength of original gratings after binarization. It can be shown that the binarized function still has  $\approx 64\%$  of its intensity in the original gratings (see Section S2 in the Supporting Information). Each grating after binarization has an effective amplitude equal to  $\Delta n_{i,b} = 2\Delta n(\pi N)^{-1/2}$  (see Sections S1 and S2 in the Supporting Information). The binarization also introduces additional Bragg peaks in Fourier space that take the residual  $\approx 36\%$  of the intensity. However, for a large number

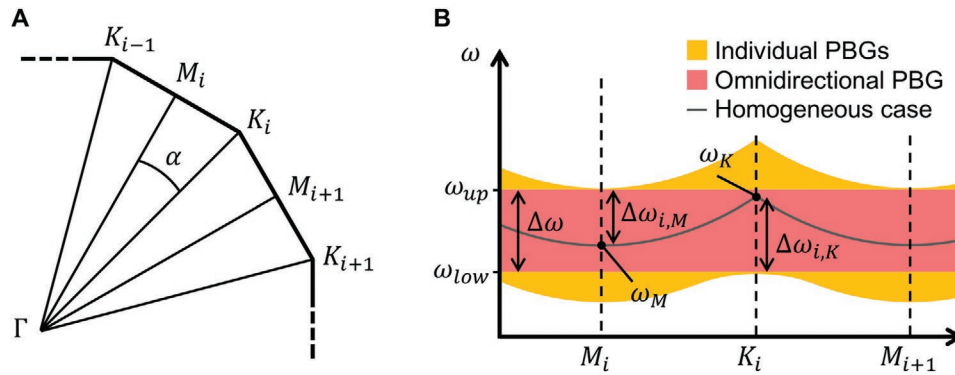


**Figure 2.** A) Schematic representation of a section of the effective Brillouin zone of the 2D quasiperiodic structure. B) Schematic band diagram showing the effective bandgaps in different directions. The bands depicted in gray show the band positions for the empty lattice case, when the grating contrast converges to zero. The orange shaded area represents the bandgap opening when a finite contrast is assumed. At the  $K$ -points, the neighboring gratings interact, which leads to a smoothing at the lower band edge and, thus, to a larger bandgap opening. The red shaded area represents the omnidirectional PBG.

of gratings, these peaks are so densely distributed that for a finite structure size they cannot be differentiated anymore (see Figure 1C). Thus, we efficiently utilize the RI contrast of the binarized structure to generate the required Bragg peak distribution.

### 3. CPBG Estimation

While every individual grating has a bandgap in its normal direction, other directions see an upshifted bandgap, corresponding to the Bragg condition. Thus, in the direction between two Bragg peaks the bandgap appears at a slightly larger frequency. An omnidirectional bandgap for one polarization is achieved when the directional bandgaps have a sufficient opening to overlap. The effective Brillouin zone of the structure is schematically shown in Figure 2A. We label the direction toward the Bragg peak of the grating with index  $i$  as  $\Gamma M_i$  and the direction between the two Bragg peaks with indices  $i$  and  $i + 1$  as  $\Gamma K_i$ . Scanning the band diagram along the edge of the effective Brillouin zone the omnidirectional PBG opening can be evaluated (Figure 2B). To achieve an omnidirectional PBG the upper edge of the PBG in  $\Gamma M_i$ -direction should be above the lower edge of the PBG in  $\Gamma K_i$ -direction.

At the  $M$ -points we neglect the interaction between different, e.g., neighboring gratings in the calculation of the directional bandgap of the single grating. At the  $K$ -points, the neighboring gratings are contributing to the bandgap opening. Neglecting the influence of other gratings beyond the next neighbors, it can be shown that the PBG opening is by a factor  $m^{1/2}$  larger than for a single grating, where  $m$  is the number of interacting gratings (2 or 3 for 2D or 3D structures, respectively; see Section S3 in the Supporting Information). Similar to the calculation in a nonbinarized structure,<sup>[33]</sup> we end up with the following expression for the relative omnidirectional PBG opening (Section S4, Supporting Information):

$$\frac{\Delta\omega}{\omega} = \frac{\omega_{up} - \omega_{low}}{\omega} = \frac{\omega_M + \Delta\omega_{i,M} - (\omega_K - \Delta\omega_{i,K})}{\omega} = \frac{1 + \sqrt{m}}{\sqrt{\pi}} \frac{\Delta n}{\bar{n}\sqrt{N}} - \frac{\alpha^2}{2} \quad (3)$$

where  $\omega_{up}$  and  $\omega_{low}$  are the upper and lower frequency edges of the CPBG,  $\omega_M$  and  $\omega_K$  are the bandgap center frequencies of

the respective directional bandgaps,  $\Delta\omega_{i,M}$  and  $\Delta\omega_{i,K}$  denote the respective directional half bandgap openings, and  $\alpha$  is the angle between  $\Gamma M_i$ - and  $\Gamma K_i$ -directions (see Figure 2). Then  $\alpha$  can be expressed in terms of the number of gratings  $N$  to arrive at a function of the RI contrast and the grating number only. However, the relation of these quantities is different for 2D and 3D.

The uniform distribution of the gratings in 2D is straightforward and leads to the relation  $\alpha = \pi/(2N)$ . The resulting expression yields the relative omnidirectional PBG opening that reaches a maximum for a certain number of gratings

$$N_{2D,opt} \approx 2.36 \left( \frac{\bar{n}}{\Delta n} \right)^{2/3}; \quad \frac{\Delta\omega_{2D}}{\omega} (N_{2D,opt}) \approx 0.67 \left( \frac{\Delta n}{\bar{n}} \right)^{4/3} \quad (4)$$

Significantly, the bandgap opening will converge to zero as the contrast goes to zero, but for finite contrast values there will always be a finite omnidirectional PBG width.

To find a connection between the angle  $\alpha$  and the grating number  $N$  in the 3D case, we make the approximation that each Bragg peak has exactly six neighbors at equal distance in reciprocal space. In reality, the sphere cannot be covered by equal hexagons. The distribution close to this approximation would be the one with a Goldberg polyhedron as its effective Brillouin zone, which would also have 12 pentagonal faces and differently sized hexagons.<sup>[40,41]</sup> Thus, our assumption slightly underestimates the maximal angle. Using this assumption, we obtain the connection  $\alpha^2 = 4\pi/(3^{3/2}N)$  (see Section S5 in the Supporting Information). As in the 2D case, there is an optimum grating number and a corresponding optimum bandgap opening

$$N_{3D,opt} \approx 2.46 \left( \frac{\bar{n}}{\Delta n} \right)^2; \quad \frac{\Delta\omega_{3D}}{\omega} (N_{3D,opt}) \approx 0.49 \left( \frac{\Delta n}{\bar{n}} \right)^2 \quad (5)$$

Again, the predicted bandgap persists even for a small but finite RI contrast.

In order for a PBG to be complete, it needs to inhibit propagation for all possible light polarizations. In 2D, the polarizations are fully described by an orthogonal basis of transverse electric (TE) and transverse magnetic (TM) polarizations. For low-refractive-index media, the shift between the bandgaps

observed in TE and TM excitations is mainly caused by the different effective mean RI of the structure. For TM-polarized light, the electric field is always tangential to the material boundaries and therefore continuous. For TE-polarized light, the  $E$  and  $D$  fields can have all orientations toward the boundaries. However, in order to find the maximum difference between the effective permittivities for the two polarizations, we may assume that all TE fields are normal to the boundaries. For that case, the relative difference in the bandgap positions for the different polarizations depends on the RI as (see Section S6 in the Supporting Information)

$$\frac{\Delta\omega_p}{\omega} = 2 \left( \frac{\Delta n}{\bar{n}} \right)^2 \quad (6)$$

In the 2D case, the discrepancy between the bandgap positions for TM and TE polarizations decreases faster than the maximal bandgap width for decreasing RI contrast. Thus, for low-RI contrasts a better overlap of the bandgaps and thus a CPBG can be expected. For 3D structures the scaling power law with an exponent of 2 is the same, and a better estimation is required to predict the existence of a CPBG. At the same time, the assumption that electric fields are only either parallel or orthogonal to interfaces represents an extreme case that will not be present in real field distributions. Therefore, in reality the birefringence will be smaller in the 3D structures, and it might be that obtaining a CPBG is still possible.

#### 4. Simulation of the 2D Case

Simulations were done using the time domain solver of CST Studio Suite.<sup>[42]</sup> A line dipole emitter was placed in the center of the proposed structure. Several other positions next to the center were also checked. While this changes the overall emission level depending on the local environment of the dipole, the relative suppression inside the bandgap itself is hardly influenced. The orientation of the dipole was changed to excite either TE (dipole in-plane) or TM (dipole out-of-plane) polarization. The lateral directions are terminated by open boundaries acting as perfect absorbers. To probe the local density of states (LDOS), we evaluate the emitted power of the dipole  $P$  by measuring the real part of its radiation impedance.<sup>[43–45]</sup> The results are then normalized to the dipole emission  $P_0$  into a homogeneous medium with the mean refractive index of the structure. A suppression of the LDOS, and therefore of the power emission, is expected for frequencies inside the PBG. It is also expected that the LDOS at these frequencies decreases exponentially with the lateral side length  $L$  of the simulation volume.<sup>[32,46]</sup> As the results are scale independent, the side lengths are normalized to the grating period,  $L/a$ .

The normalized TM power emission spectrum of the dipole for four different structure sizes with 16 gratings and a small RI contrast of  $n_1/n_2 = 1.58/1.42 \approx 1.11$  is shown in Figure 3. An emission suppression band is seen in the spectra at a normalized frequency of about 0.493. The maximal suppression shows the expected exponential decay with increasing side length of the square-shaped simulated structure (inset in Figure 3).

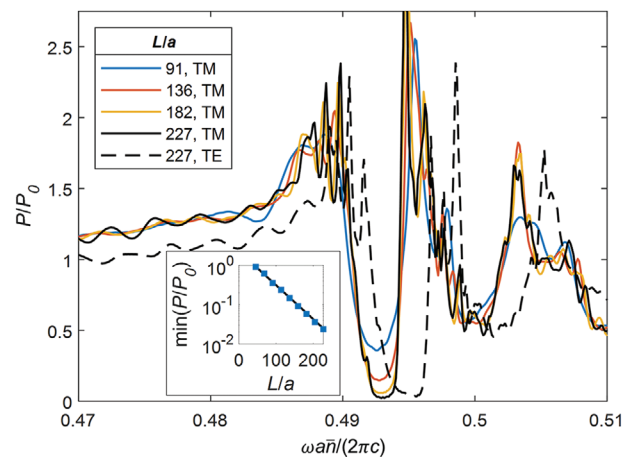


**Figure 3.** Normalized power emission  $P/P_0$  of a dipole placed inside a square-shaped 2D quasiperiodic structure. The  $L/a$  values specifying the side length of the structure are rounded to integer values. The structure size is varying from 91 to 227 lattices constants. The solid lines represent emission for TM excitation; the dashed line represents TE excitation. The structure has an RI contrast  $n_1/n_2 = 1.58/1.42 \approx 1.11$  and  $N = 16$  underlying gratings. Inset: Semilogarithmic plot of the minima of the normalized TM power emission over the edge length. The black line is an exponential fit showing as a straight line in the semi-logarithmic plot.

Additionally, for a CPBG the suppression experienced by different polarizations should coincide spectrally. Although a slight spectral shift between the TM and TE positions of the emission gap is observed (Figure 3), there is a clear overlap region corresponding to a polarization-independent CPBG. The overlap should further improve for smaller index contrast as the polarization shift (Equation (6)) converges more rapidly than the individual bandgap openings (Equation (4)). In combination, these results unambiguously confirm the opening of a CPBG.

The predicted and simulated bandgap sizes were compared for several grating numbers (Section S7, Supporting Information). We find deviations from our model in three aspects: i) for large grating numbers the bandgap vanishes. ii) The optimum grating number is slightly shifted toward smaller grating numbers. iii) The bandgaps are narrower than expected in nearly all simulations. However, the results confirm that there is indeed an optimum condition for the number of gratings and that our model does predict the overall trend of the dependence.

#### 5. Simulation of the 3D Case

The gratings for the 3D structures need to be arranged such that the Bragg peaks are homogeneously distributed as points on the spherical surface with radius  $b = 2\pi/a$ , and the maximal distance from any point on the sphere to the closest Bragg peak is minimized. This task is a special type of a sphere covering problem where no exact solution exists for an arbitrary number of points.<sup>[41]</sup> There are, however, solutions available in table form that are putatively optimal.<sup>[47]</sup> Since each grating produces two Bragg peaks on opposite sides of the sphere, a point symmetric distribution is necessary. The arrangements used for this work were the icosahedral solutions to the covering problem

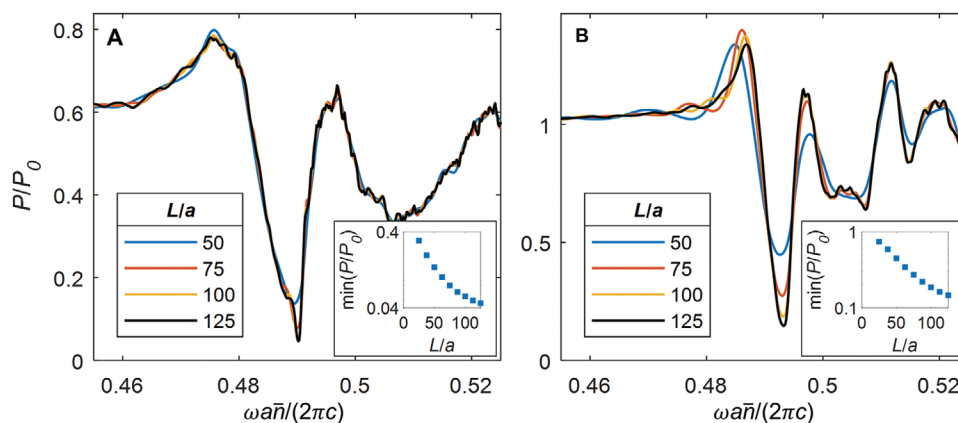


**Figure 4.** Normalized emitted power spectrum of a dipole placed inside a 3D quasiperiodic structure based on an icosahedral distribution of the underlying gratings. A) For the simulation, an RI contrast of  $n_1/n_2 = 1.6/1$  and a grating number of  $N = 46$  were used. B) For the simulation, the contrast was  $1.38/1$  and the grating number was 81. The structure size is varying from 50 to 125 lattice constants. The spectra are normalized to the dipole emission in a homogeneous medium with the mean refractive index,  $\bar{n} = 1.3$  in panel (A) and 1.19 in panel (B). Insets: Semilogarithmic plot of the minima of the normalized power emission over the edge length.

calculated in ref. [47]. For the results shown here the distributions of 92 and 162 points were used, corresponding to 46 and 81 gratings, respectively. The former value corresponds to the optimum for the used RI values as calculated by Equation (5). The latter is slightly adjusted to a lower grating number in accordance with the deviations seen between the 2D theoretical model and the simulation results (Section S7, Supporting Information). The point distributions are listed in Tables S1 and S2 (Supporting Information).

The simulation of low-contrast 3D structures requires large simulation volumes, which quickly leads to unbearable computing efforts. We have therefore limited our consideration to structures with relatively large RI contrasts of  $n_1/n_2 = 1.6/1$  and  $1.38/1$  with a maximum cube side length of 125 lattice constants. The simulation yields a clear gap in the emission spectrum of the dipole (see Figure 4). We did not observe an exponential decay of the emitted power over the side length  $L$ . Instead, based on extrapolation of the structure size, the emission suppression in both cases saturates at  $\approx -10$  dB relative to the low-frequency level. The normalized power emission  $P/P_0$  at low frequency is different for the two structures due to different local dipole positions and orientations. These local properties do not change the relative suppression scaling with the size of the structure.

The theory predicts a CPBG, and thus an unlimited LDOS suppression, which is not seen in the 3D simulations. Apparently in the presented 3D structure, some channels are still present where energy propagates without evanescent decay. In the far-field emission pattern, we also observe some emission directions that are not predicted by the theory. The far-field results are presented in Section S8 (Supporting Information). These deviations could be due to several reasons: first, the chosen RI contrast might still be too large for the analytical approximation to be applicable. Second, the interaction between gratings might not be negligible. A higher-order theory is required to take these effects into account. Third, it might also be that polarization effects are the limiting factor. According to the estimation, the polarization effects can close the PBG as the bandgap opening and the polarization splitting both scale with

the square of the RI contrast in 3D structures (Equations (5) and (6)). The effect of polarization should be further studied by simulations using the scalar wave approximation and therefore eliminating the influence of polarization effects in the proposed structures.

## 6. Experimental Realization

The 3D structures were also realized and measured experimentally in the microwave range. The structures were produced by 3D printing of polylactide (PLA) plastic, which has a permittivity of  $\approx 2.54$  ( $n \approx 1.59$ ) and nearly no losses ( $\tan(\delta) \approx 10^{-2}$ ) in the microwave range.<sup>[48]</sup> The scaling of the structures was done such that the theoretically predicted CPBG lies at 40 GHz. For a mean refractive index of  $\approx 1.3$ , the corresponding period of the structure is  $a = 2.825$  mm. The relative size of the structure is about  $50 \times 50 \times 25$  lattice constants, and the underlying grating distribution is the same as in the simulation for 1.6 RI contrast. The printing procedure is described in Section S9 (Supporting Information). A photograph of the printed structure is shown in the inset in Figure 5A.

Transmission instead of emission was measured as in previous publications.<sup>[21,27,28]</sup> Emission measurements require an antenna to be placed inside the structure and a corresponding feed line. This is difficult to achieve without creating additional channels for emission. The transmissivity of the structure was measured in the solid angle range of  $\pm 30^\circ$  in azimuth and elevation (corresponding to  $\approx \pm 22^\circ$  inside the structure, corrected for refraction) and a frequency range of 30–50 GHz (Section S10, Supporting Information).

Figure 5A shows an average transmission spectrum, where for each frequency point the transmission was averaged over the full angular range. By this we get a representative average over different crystallographic directions. The graph shows a clear edge at  $\approx 38$  GHz, which is close to the expected bandgap position. The transmission does not have a peak close to the transmission gap and does not recover at higher frequencies, which is different to the emission spectra. This is an important

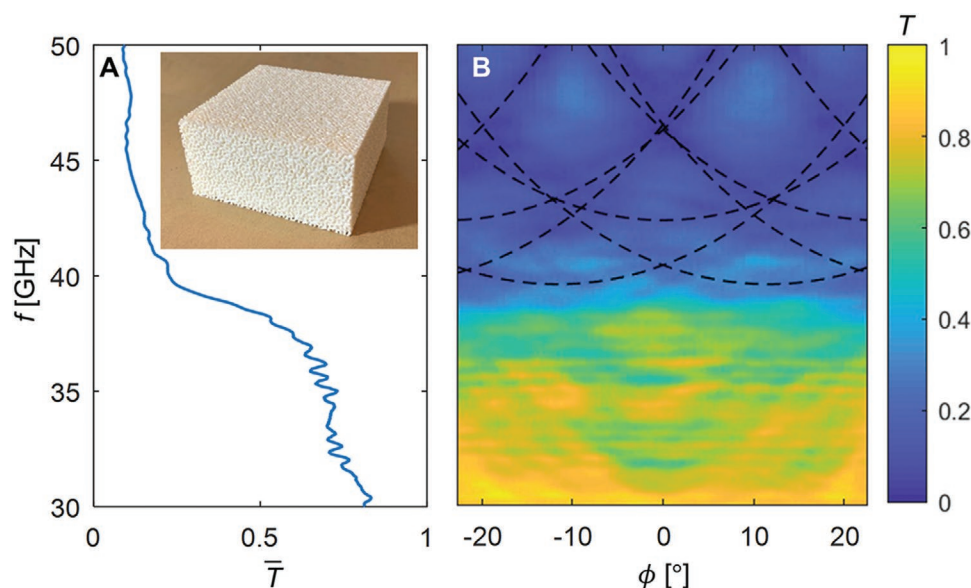


**Figure 5.** Transmission measurements over frequency. A) Transmission of the structure averaged over the full measured angular range of  $\pm 30^\circ$  in azimuth and elevation. A transmission suppression of about  $-6$  dB is seen at the transition of around 40 GHz. Inset: Photography of the 3D-printed structure. B) Measured transmission at  $\theta = 0$  over frequency and  $\phi$ . The  $\phi$  values inside the structure are shown, corrected for refraction at the interface. The dashed black lines represent the Bragg condition of neighboring gratings for an assumed mean refractive index of  $\bar{n} = 1.34$ .

and expected difference between transmission and emission results. Emission is sensitive to the density of states in the structured material. It increases at the band edges due to slow light propagation and decreases in the bandgaps. Transmission is low in the bandgap, too, but in contrast to emission it is also low when the group velocity is small or when light is deflected by the structure. Thus, there is no peak at the lower and upper frequency band edges. On the high-frequency side of the bandgap, there is reflection due to higher-order bandgaps and reflection and deflection due to group velocity effects. This behavior can equivalently be observed in transmission simulations (Section S11, Supporting Information).

The relative suppression at the bandgap frequency in emission simulations and transmission measurements is found by comparison to the corresponding values at lower frequencies. From Figure 5A a transmission suppression of about  $-6$  dB is seen at 41 GHz as compared to 30 GHz. In emission simulations, we expect a comparable suppression by taking a volume with a distance between the dipole and the boundary of the simulation volume, which equals the slab thickness in the transmission measurement. This is the case for the structure with  $L/a = 50$  in Figure 4A. A comparable suppression of about  $-6$  dB in the minimum is observed relative to the emission level at a normalized frequency of 0.46. The quasiperiodic structure constitutes an almost angle-independent low-pass filter for microwave radiation.

The residual angle dependence in the stop band can be traced back to the neighboring Bragg peaks (Figure 5B). The dashed black lines represent the Bragg condition of the several Bragg peaks close to normal direction. They fit the measured data very well for an assumed mean refractive index of 1.34. This is slightly above the expected value of  $\approx 1.3$ . We assign this deviation to a slightly higher solid filling fraction of the structure caused by the model preparation during the 3D printing procedure.

The angle-resolved measurement also confirms the effective Bragg gratings underlying the seemingly disordered structure. When measuring the transmission at frequencies slightly below and above the CPBG range, it is expected that light is transmitted only in certain identifiable directions. At frequencies slightly below the CPBG (below  $\omega_{\text{low}}$ , see Figure 2B), transmission in the Bragg grating directions (corresponding to the  $M$ -directions, see Figure 2A) is already blocked, while light can still propagate in the directions in between the Bragg peaks ( $K$ -directions). At frequencies slightly above the CPBG (above  $\omega_{\text{up}}$ ) this behavior is inverted. In between the Bragg peaks, transmission should now be blocked, while in the grating directions no bandgap is available. This behavior is well visible in measurements at 39 and 40.5 GHz, respectively. The measurement data in comparison to the Bragg peak positions are shown in Figure 6A,D. For frequencies inside the bandgap, the transition between these two cases can be seen (Figure 6B,C). The incidence angles displayed in Figure 6 were corrected for the refraction in the quasicrystal structure using the average refractive index.

## 7. Conclusion

We have proposed a distributed quasiperiodic structure with an efficient utilization of the RI contrast to block emission in all directions. In contrast to previous studies, an analytical model has been presented, which predicts optimum conditions for the maximum bandgap opening for both the 2D and the 3D case. At these optimum conditions, a bandgap opening for an arbitrarily small RI contrast is expected. We have shown numerically that it is possible to obtain a 2D CPBG with an RI contrast as low as 1.11. This is the smallest RI contrast producing a CPBG that was demonstrated so far. Even a typical RI

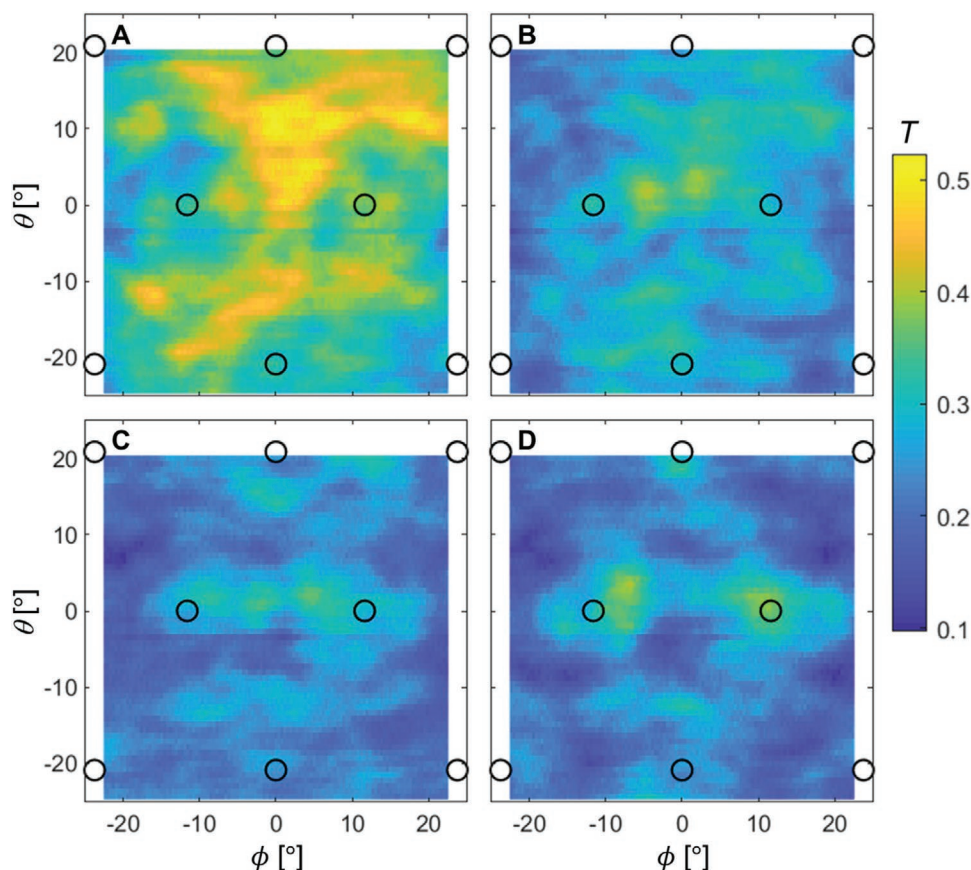


**Figure 6.** Measured transmission for different angles inside the structure at frequencies A) 39 GHz, B) 39.5 GHz, C) 40 GHz, and D) 40.5 GHz, which is slightly A) below, B,C) inside, and D) slightly above the expected CPBG frequency range. The black circles show the expected Bragg peaks of the gratings underlying the measured structure. Angles inside the structure are shown, corrected for refraction at the interface.

contrast in the order of 1.1 between the ordinary and extraordinary polarizations of a typical liquid crystal<sup>[49]</sup> would be sufficient to open a CPBG.

In 3D simulation, we have demonstrated almost  $-10$  dB suppression of emission at contrasts of 1.6 and 1.38 that could be realized with low-index materials such as polymers and glasses. This, by far, exceeds the suppression shown in previous works investigating 3D structures at similar contrasts.<sup>[50,51]</sup> Further adjustment of the theory might lead to the design of structures with even higher suppression. We have also manufactured the 3D structures by additive manufacturing with standard 3D-printing techniques and conducted transmission measurements in the microwave range. Thereby, we were able to confirm a strong and nearly direction-independent transmission suppression at the expected CPBG position and verify the quasiperiodic nature of the investigated structures. We envisage our approach to pave the way for further artificial low-index materials with unprecedented properties.

## Supporting Information

Supporting Information is available from the Wiley Online Library or from the author.

## Acknowledgements

The authors acknowledge the support from Dassault Systemes with their CST Studio Suite software. Funding is made by Deutsche Forschungsgemeinschaft (DFG) (Project No. 278744289). The experimental studies have been supported by the grant of Russian Science Foundation (Grant No. 20-79-10316).

Open access funding enabled and organized by Projekt DEAL.

## Conflict of Interest

The authors declare no conflict of interest.

## Data Availability Statement

The data that support the findings of this study are available from the corresponding author upon reasonable request.

## Keywords

additive technology, low-index artificial materials, low-index complete photonic bandgap, reciprocal space engineering, wave localization

Received: April 18, 2021  
Revised: August 18, 2021  
Published online: October 18, 2021

- [1] E. Yablonovitch, *Phys. Rev. Lett.* **1987**, *58*, 2059.
- [2] S. John, *Phys. Rev. Lett.* **1987**, *58*, 2486.
- [3] J. D. Joannopoulos, P. R. Villeneuve, S. Fan, *Nature* **1997**, *386*, 143.
- [4] J. D. Joannopoulos, S. G. Johnson, J. N. Winn, R. D. Meade, *Photonic Crystals: Molding the Flow of Light*, 2nd ed., Princeton University Press, Princeton, NJ **2008**.
- [5] W. Cai, V. Shalae, *Optical Metamaterials*, Springer, New York, NY **2010**.
- [6] N. I. Zheludev, Y. S. Kivshar, *Nat. Mater.* **2012**, *11*, 917.
- [7] S. Molesky, Z. Lin, A. Y. Piggott, W. Jin, J. Vucković, A. W. Rodriguez, *Nat. Photonics* **2018**, *12*, 659.
- [8] W. Li, F. Meng, Y. Chen, Y. Li, X. Huang, *Adv. Theory Simul.* **2019**, *2*, 1900017.
- [9] S. D. Campbell, D. Sell, R. P. Jenkins, E. B. Whiting, J. A. Fan, D. H. Werner, *Opt. Mater. Express* **2019**, *9*, 1842.
- [10] F. Meng, X. Huang, B. Jia, *J. Comput. Phys.* **2015**, *302*, 393.
- [11] W. Ma, Z. Liu, Z. A. Kudyshev, A. Boltasseva, W. Cai, Y. Liu, *Nat. Photonics* **2021**, *15*, 77.
- [12] D. S. Wiersma, *Nat. Photonics* **2013**, *7*, 188.
- [13] S. Yu, C.-W. Qiu, Y. Chong, S. Torquato, N. Park, *Nat. Rev. Mater.* **2021**, *6*, 226.
- [14] P. M. Piechulla, L. Muehlenbein, R. B. Wehrspohn, S. Nanz, A. Abass, C. Rockstuhl, A. Sprafke, *Adv. Opt. Mater.* **2018**, *6*, 1701272.
- [15] G. Shang, M. Eich, A. Petrov, *APL Photonics* **2020**, *5*, 060901.
- [16] A. D. Sinelnik, I. I. Shishkin, X. Yu, K. B. Samusev, P. A. Belov, M. F. Limonov, P. Ginzburg, M. V. Rybin, *Adv. Opt. Mater.* **2020**, *8*, 2001170.
- [17] P. Wang, Y. Zheng, X. Chen, C. Huang, Y. V. Kartashov, L. Torner, V. V. Konotop, F. Ye, *Nature* **2020**, *577*, 42.
- [18] N. Lassaline, R. Brechbühler, S. J. W. Vonk, K. Ridderbeek, M. Spieser, S. Bisig, B. L. Feber, F. T. Rabouw, D. J. Norris, *Nature* **2020**, *582*, 506.
- [19] Y. Cao, V. Fatemi, A. Demir, S. Fang, S. L. Tomarken, J. Y. Luo, J. D. Sanchez-Yamagishi, K. Watanabe, T. Taniguchi, E. Kaxiras, R. C. Ashoori, P. Jarillo-Herrero, *Nature* **2018**, *556*, 80.
- [20] Y. Cao, V. Fatemi, S. Fang, K. Watanabe, T. Taniguchi, E. Kaxiras, P. Jarillo-Herrero, *Nature* **2018**, *556*, 43.
- [21] W. Man, M. Megens, P. J. Steinhardt, P. M. Chaikin, *Nature* **2005**, *436*, 993.
- [22] H. Men, K. Y. K. Lee, R. M. Freund, J. Peraire, S. G. Johnson, *Opt. Express* **2014**, *22*, 22632.
- [23] A. Cerjan, S. Fan, *Phys. Rev. A* **2017**, *96*, 051802.
- [24] P. R. Villeneuve, M. Piché, *Phys. Rev. B* **1992**, *46*, 4969.
- [25] K. M. Ho, C. T. Chan, C. M. Soukoulis, *Phys. Rev. Lett.* **1990**, *65*, 3152.
- [26] L. Chen, K. A. Morgan, G. A. Alzaidy, C.-C. Huang, Y.-L. D. Ho, M. P. C. Taverne, X. Zheng, Z. Ren, Z. Feng, I. Zaimpekis, D. W. Hewak, J. G. Rarity, *ACS Photonics* **2019**, *6*, 1248.
- [27] W. Man, M. Florescu, K. Matsuyama, P. Yadak, G. Nahal, S. Hashemizad, E. Williamson, P. Steinhardt, S. Torquato, P. Chaikin, *Opt. Express* **2013**, *21*, 19972.
- [28] M. E. Zoorob, M. D. B. Charlton, G. J. Parker, J. J. Baumberg, M. C. Netti, *Nature* **2000**, *404*, 740.
- [29] X. Zhang, Z.-Q. Zhang, C. T. Chan, *Phys. Rev. B* **2001**, *63*, 81105.
- [30] L. Dal Negro, S. V. Boriskina, *Laser Photonics Rev.* **2012**, *6*, 178.
- [31] M. Florescu, S. Torquato, P. J. Steinhardt, *Proc. Natl. Acad. Sci. USA* **2009**, *106*, 20658.
- [32] C. Rockstuhl, F. Lederer, *Phys. Rev. B* **2009**, *79*, 132202.
- [33] P. L. Hagelstein, D. R. Denison, *Opt. Lett.* **1999**, *24*, 708.
- [34] P. N. Dyachenko, Y. V. Miklyaev, *Proc. SPIE* **2006**, *6182*, 618221.
- [35] M. C. Rechtsman, H.-C. Jeong, P. M. Chaikin, S. Torquato, P. J. Steinhardt, *Phys. Rev. Lett.* **2008**, *101*, 73902.
- [36] R. C. Gauthier, A. Ivanov, *Opt. Express* **2004**, *12*, 990.
- [37] N. D. Lai, W. P. Liang, J. H. Lin, C. C. Hsu, C. H. Lin, *Opt. Express* **2005**, *13*, 9605.
- [38] N. F. Berk, *Phys. Rev. A* **1991**, *44*, 5069.
- [39] L. Maiwald, S. Lang, D. Jalas, H. Renner, A. Y. Petrov, M. Eich, *Opt. Express* **2018**, *26*, 11352.
- [40] M. Goldberg, *Tohoku Math. J.* **1937**, *43*, 104.
- [41] E. B. Saff, A. B. J. Kuijlaars, *Math. Intell.* **1997**, *19*, 5.
- [42] More information available at <https://www.3ds.com/products-services/simulia/products/cst-studio-suite> (accessed: August **2021**).
- [43] A. E. Krasnok, A. P. Slobozhanyuk, C. R. Simovski, S. A. Tretyakov, A. N. Poddubny, A. E. Miroshnichenko, Y. S. Kivshar, P. A. Belov, *Sci. Rep.* **2015**, *5*, 12956.
- [44] K. M. Schulz, H. Vu, S. Schwaiger, A. Rottler, T. Korn, D. Sonnerberg, T. Kipp, S. Mendach, *Phys. Rev. Lett.* **2016**, *117*, 85503.
- [45] K. M. Schulz, D. Jalas, A. Y. Petrov, M. Eich, *Opt. Express* **2018**, *26*, 19247.
- [46] A. D. Villa, S. Enoch, G. Tayeb, V. Pierro, V. Galdi, F. Capolino, *Phys. Rev. Lett.* **2005**, *94*, 183903.
- [47] R. H. Hardin, N. J. A. Sloane, W. D. Smith, Tables of spherical codes with icosahedral symmetry, <http://neilsloane.com/icosahedral.codes> (accessed: August **2021**).
- [48] G. Boussatour, P.-Y. Cresson, B. Genestie, N. Joly, T. Lasri, *IEEE Microw. Wireless Compon. Lett.* **2018**, *28*, 374.
- [49] J. Li, C.-H. Wen, S. Gauza, R. Lu, S.-T. Wu, *J. Disp. Technol.* **2005**, *1*, 51.
- [50] M. J. Ventura, M. Gu, *Adv. Mater.* **2008**, *20*, 1329.
- [51] H. Yin, B. Dong, X. Liu, T. Zhan, L. Shi, J. Zi, E. Yablonovitch, *Proc. Natl. Acad. Sci. USA* **2012**, *109*, 10798.
- [52] The peak prominence (Section S7, Supporting Information) is defined in the MATLAB documentation, <https://www.mathworks.com/help/signal/ug/prominence.html> (accessed: August 2021).